J Seismol
DOI 10.1007/s10950-008-9090-6

ORIGINAL ARTICLE

Broadband strong motion simulation in layered half-space using stochastic Green's function technique

Y. Hisada

Received: 30 March 2007 / Accepted: 7 January 2008

Abstract The stochastic Green's function method, which simulates one component of the far-field S-waves from an extended fault plane at high frequencies (Kamae et al., *J Struct Constr Eng Trans AIJ*, 430: 1–9, 1991), is extended to simulate the three components of the full waveform in layered half-spaces for broadband frequency range. The method firstly computes ground motions from small earthquakes, which correspond to the ruptures of sub-faults on a fault plane of a large earthquake, and secondly constructs the strong motions of the large earthquake by superposing the small ground motions using the empirical Green's function technique (e.g., Irikura, *Proc 7th Japan Earthq Eng Symp*, 151–156, 1986). The broadband stochastic omega-square model is proposed as the moment rate functions of the small earthquakes, in which random and zero phases are used at higher and lower frequencies, respectively. The zero phases are introduced to simulate a smooth ramp function of the moment function with the duration of 1/fc s (fc: the corner frequency) and to reproduce coherent strong motions at low frequencies (i.e., the directivity pulse). As for the radiation coefficients, the theoretical values of double couple sources for lower frequencies and the theoretical isotropic values for the P-, SV-, and SH-waves (Onishi and Horike, *J Struct Constr Eng Trans AIJ*, 586:37–44, 2004) for high frequencies are used. The proposed method uses the theoretical Green's functions of layered half-spaces instead of the far-field S-waves, which reproduce the complete waves including the direct and reflected P- and S-waves and surface waves at broadband frequencies. Finally, the proposed method is applied to the 1994 Northridge earthquake, and results show excellent agreement with the observation records at broadband frequencies. At the same time, the method still needs improvements especially because it underestimates the high-frequency vertical components in the near fault range. Nonetheless, the method will be useful for modeling high frequency contributions in the hybrid methods, which use stochastic and deterministic methods for high and low frequencies, respectively (e.g., the stochastic Green's function method+finite difference methods; Kamae et al., *Bull Seism Soc Am*, 88:357–367, 1998; Pitarka et al., *Bull Seism Soc Am* 90:566–586, 2000), because it reproduces the full waveforms in layered media including not only random characteristics at higher frequencies but also theoretical and deterministic coherencies at lower frequencies.

Keywords Broadband strong motion simulation · Omega-squared model · Green's function of layered half-spaces · Stochastic Green's function method · Empirical Green's function method · The scaling law · 1994 Northridge earthquake

---

Y. Hisada (✉)
Department of Architecture, Kogakuin University,
Nishi-Shinjuku 1-24-2, Shinjuku,
Tokyo 163-8677, Japan
e-mail: hisada@cc.kogakuin.ac.jp

1 Introduction

Hybrid methods that combine deterministic and stochastic estimations for lower and higher frequencies are widely used to simulate broadband strong ground motions (e.g., Kamae et al. 1998; Pitarka et al. 2000). The matching frequencies between the two estimations are usually around 0.5–2 Hz, which are the most important frequency range for engineering structures. However, the two estimations sometimes show large differences in amplitudes, arrival times, and waveforms in that frequency range because of completely different methodologies. Two approaches have been proposed to remedy this problem and connect the two results more smoothly. One approach is to introduce stochastic randomness in deterministic methods at higher frequencies. For example, Herrero and Bernard (1994) proposed the *k*-squared model, which is an omega-squared model based on a kinematic fault model using randomness in slip distribution at higher frequencies. Hisada (2000, 2001) modified the model by introducing pseudo-dynamic slip and the *k*-squared random distributions not only in slip but also in rupture time at higher frequencies. More recently, various similar models considering pseudo-dynamic slips and randomness for slip and rupture time (or rupture velocity) have been proposed (e.g., Guatteri et al. 2004; Hartzell et al. 2005). These approaches are theoretically sound, but rather time consuming and not efficient at very high frequencies, especially when considering realistic layered half-spaces, because huge numbers of Green's functions are necessary to maintain the continuity of the rupture front (about 8–10 source points per wavelength).

The second approach introduces deterministic coherency in stochastic methods at lower frequencies. Kamae et al. (1991) proposed the stochastic Green's function method, in which the far-field S-waves from the stochastic point source (Boore 1983) are superposed on an extended fault plane using the empirical Green's function technique (Irikura 1986). To extend this method to lower frequencies, Kagawa (2004) proposed a trial-and-error technique, in which several stochastic Green's functions are simulated, and one can choose synthetics that are consistent with deterministic results. Onishi and Horike (2004) improved the method by introducing the theoretical radiation coefficients of the P-, SV-, and SH-waves and a ray tracing technique in layered half-spaces. These stochastic approaches are much faster to compute than the theoretical approaches because it basically requires only one source point per sub-fault using simple Green's functions.

The purpose of this paper is to improve the stochastic Green's function method by introducing deterministic coherencies at lower frequencies and by computing the complete Green's functions of layered half-spaces. First, we propose the broadband stochastic omega-square model, whose phases are random at higher frequencies and zero at lower frequencies, to reproduce both the random characteristics at higher frequencies and the deterministic coherencies (e.g., the directivity pulses) at lower frequencies. Second, we introduce the theoretical Green's function of layered half-spaces using the wavenumber integration technique based on the reflection/transmission (R/T) matrix (Hisada 2001), which is numerically stable up to very high frequencies. Third, we propose a method to compute the theoretical P-, SV-, and SH-radiations at high frequencies (Onishi and Horike 2004), by introducing P-, SV-, and SH-sources. Finally, we check the validity of the method by comparing observations with results from simulations for the 1994 Northridge earthquake.

2 Formulation of the broadband stochastic Green's function method in layered half-space

2.1 Formulation of the stochastic Green's function method

We briefly explain the original stochastic Green's function method (Kamae et al. 1991; see also Kamae et al. 1998). In the method, one first generates ground motions from small earthquakes, which correspond to sub-faults of a large earthquake as shown in Fig. 1. Next, one constructs the strong motions of the large earthquake by superimposing those of the small earthquakes, using the empirical Green's function technique (Irikura 1986; Yokoi and Irikura 1991).

Although the original formulation is written in the time domain, we will express it in the frequency domain, as follows:

$$U_k^{\mathrm{L}}(\omega) = \sum_{\xi=1}^{N} \sum_{\eta=1}^{N} F(\omega) \cdot C_{\xi\eta} \cdot U_{k\xi\eta}^{\mathrm{S}}(\omega) \cdot \exp\left(i\omega \cdot t_{\xi\eta}\right) \quad (1)$$

$$(k = x, y, z),$$

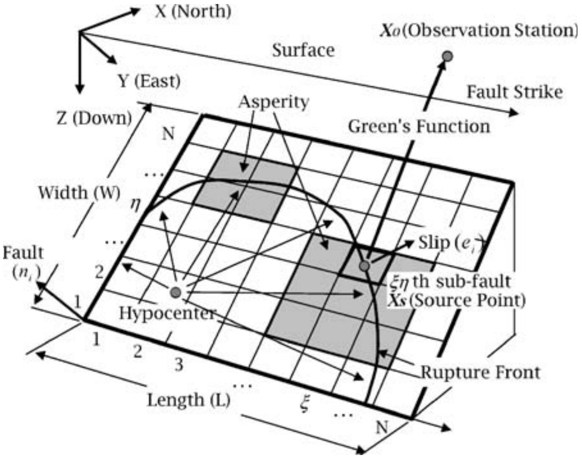

Fig. 1 Fault parameters of a large fault and sub-faults

where ω is the circular frequency, and the superscripts L and S stand for the large and small earthquakes, respectively. The subscript k corresponds to a component of the x-, y-, or z-axes. ξ and η are the sub-fault numbers along the length and the width, and $t_{\xi\mu}$ is the rupture time of the $\xi\eta$ sub-fault (see Fig. 1). The function F is introduced to modify the slip function of the small earthquakes into that of the large earthquake, as we will explain in Section 2.4. N is the number of sub-faults along the length and the width and is also the scaling parameter between the large and small earthquakes. This method assumes the following scaling relation between the small and large earthquakes (Irikura 1983; Yokoi and Irikura 1991).

$$\frac{L^{\mathrm{L}}}{L^{\mathrm{S}}} = \frac{W^{\mathrm{L}}}{W^{\mathrm{S}}} = \frac{D^{\mathrm{L}}}{D^{\mathrm{S}}} = \frac{\tau^{\mathrm{L}}}{\tau^{\mathrm{S}}} = \left(\frac{M_0^{\mathrm{L}}}{CM_0^{\mathrm{S}}}\right)^{1/3} \approx N \tag{2}$$

where, L, W, D, and τ are the length, the width, the slip, and the rise time of the faults, respectively. $C_{\xi\mu}$ and C in Eqs. 1 and 2 are the ratio of the stress drops between the large and small earthquakes (Yokoi and Irikura 1991).

$$C = \frac{\Delta\sigma^{\mathrm{L}}}{\Delta\sigma^{\mathrm{S}}} \tag{3}$$

2.2 Broadband omega-square model for small earthquakes and moment rate function

Regarding the Green's functions from small earthquakes (U_k^{S}), Irikura (1986) used observation records as semi-empirical Green's functions, whereas Kamae et al. (1991) used the stochastic Green's function of the far field S-waves in a homogeneous full-space (Boore 1983). In addition, those methods assume random phases for the source spectra; this restricts the extension to lower frequencies. We extend the method by introducing coherencies in source spectra at lower frequencies and by using the theoretical Green's function in a layered half-space.

Using the representation theorem of a point dislocation source (e.g., Aki and Richards 1980), the velocities at an observation point Y from the small earthquakes are represented as follows:

$$\dot{U}_k^{\mathrm{S}}(X_{\mathrm{O}};\omega) = \dot{M}^{\mathrm{S}}(\omega)\left(e_i n_j + e_j n_i\right) U_{ik,j}(X_{\mathrm{O}}, X_{\mathrm{S}};\omega) \tag{4}$$
$$(k = x, y, z)$$

where, X_{O} and X_{S} are observation and source points, respectively (see Fig. 1). The subscripts i, j, and k correspond to components of the x, y, or z-axes, where the summation convention is used. e_i and n_i are the ith component of the unit vectors in the fault slip and the fault normal direction, respectively. $U_{ik,j}$ is the derivative of the Green's function with respect to the jth direction. The theoretical Green's functions of the layered half-space are formulated by the wavenumber integration method based on the R/T matrix method, and easily computed even at extremely high frequencies (e.g., Hisada 1995).

$\dot{M}^{\mathrm{S}}$ in Eq. 4 is the source spectrum of a small earthquake, which is the Fourier spectrum of the moment-rate function. Assuming the omega-squared model (Brune 1970; Boore 1983), its amplitude spectrum at a frequency, f, is expressed as follows:

$$\left|\dot{M}^{\mathrm{S}}(f)\right| = \frac{M_0^{\mathrm{S}}}{1 + \left(f/f_C^{\mathrm{S}}\right)^2} P\left(f, f_{\max}^{\mathrm{S}}\right) \tag{5}$$

where, M_0^{S} is the seismic moment of the small earthquake (in dyne-cm), and is expressed as follows using Eq. 2.

$$M_0^{\mathrm{S}} \approx M_0^{\mathrm{L}}/CN^3 = \mu D^{\mathrm{L}} L^{\mathrm{L}} W^{\mathrm{L}}/CN^3 \tag{6}$$

f_C^{S} in Eq. 5 is the corner frequency (Hz), expressed as follows (Brune 1970),

$$f_C^{\mathrm{S}} = 4.9 \cdot 10^6 V_{\mathrm{S}}\left(\Delta\sigma^{\mathrm{S}}/M_0^{\mathrm{S}}\right)^{1/3} \tag{7}$$

where, V_S is the shear wave velocity of the source layer (in km/s), and $\Delta\sigma^S$ is the stress drop (in bar=0.1 MPa). The function P in Eq. 5 is a high-cut filter due to $f^S_{\max}$,

$$P(f, f_{\max}) = \frac{1}{\sqrt{1+(f/f_{\max})^{2n}}} \tag{8}$$

where, n=4 is recommended by Boore (1983). On the other hand, Tsuruki et al. (2006) proposed $f_{\max}$=6.0 Hz and n=1.55 for crustal earthquakes, using various observation data in Japan.

We propose the broadband omega-square model using not only random phases from $-\pi$ to $+\pi$ at higher frequencies but also zero phases at lower frequencies. The use of zero phases is one of the simplest techniques to reproduce a coherent moment-rate function and thus to simulate the coherent waves at low frequencies. To explain this, we first derive the theoretical moment function of the omega-square model by assuming zero phases. Equation 5 with zero phases is transformed into the following moment-rate function, using the Fourier inverse-transform.

$$\dot{M}^S(t) = \pi \cdot M^S_0 f^S_C \exp\left(-2\pi \cdot f^S_C |t|\right) \tag{9}$$

where we assume that P=1 for simplicity; numerical results show that the inclusion of P gives a smoother shape of the moment-rate function. The moment function corresponding to Eq. 9 is expressed as follows:

$$M^S(t) = \begin{cases} 0.5M^S_0 \exp\left(+2\pi \cdot f^S_C t\right), & (t \le 0) \\ 0.5M^S_0 \left\{2 - \exp\left(-2\pi \cdot f^S_C t\right)\right\}, & (t \ge 0) \end{cases} \tag{10}$$

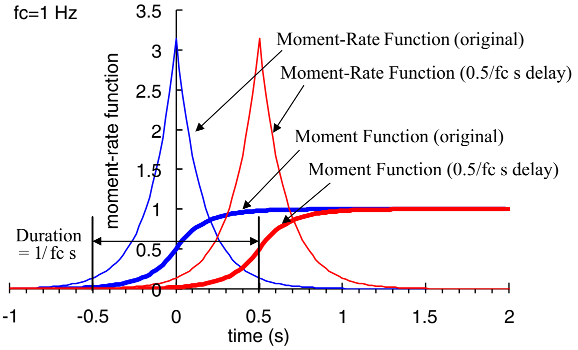

Fig. 2 Normalized moment-rate and moment functions using the omega-square model with zero phases

Figure 2 shows an example of the moment-rate function and the corresponding moment functions for the case of $f^S_C = 1$ Hz and $M^S_0 = 1$. The original moment-rate function (the thin blue line with "original" in the figure) is a simple axial symmetry function peaked at t=0 (s), and the moment function (thick blue line) is a smoothed ramp function with duration (rise time) of $1/f^S_C$ (s). Since they start at about $-0.5/f^S_C$ (s), we introduce a delay time of $+0.5/f^S_C$ (s) for actual applications, as shown by the red lines with "0.5/fc s delay" in the figure.

Next, we show an example of the broadband moment-rate and moment functions using both zero and random phases at lower and higher frequencies, respectively. Figure 3 shows results of the case for $f^S_C = 0.25$ Hz and $M^S_0 = 1$. Figure 3a is a broadband phase spectrum, in which we use random phases between $-\pi$ and $+\pi$ at frequencies higher than f_r (=2 Hz), and the phases gradually tend to zero at frequencies lower than f_r. Figure 3b shows the Fourier amplitudes of the source spectra, in which the black line is the theoretical omega-squared model of Eq. 5, and the red line represents the iterated results obtained by using the phase spectrum of Fig. 3a. Figure 3c shows the moment-rate functions with a duration of about $1/f^S_C = 4$ s, which correspond to the displacement waveforms in far-field. The black and red lines represent the results using the zero phases and the phases of Fig. 3a, respectively. In the latter result, we clip the amplitudes before t=0 (s) and negative values. Figure 3d shows the moment-functions, and Fig. 3e and f are the first- and second-order derivatives of the moment-rate functions, which correspond to the velocities and the accelerations in the far-field, respectively. The results without random phases show unrealistic waveforms, especially in the acceleration. On the other hand, the broadband omega-square model reproduces not only the coherent moment-rate and moment functions at lower frequencies (see Fig. 3c,d) but also the random waveforms at high frequencies (see Fig. 3e,f).

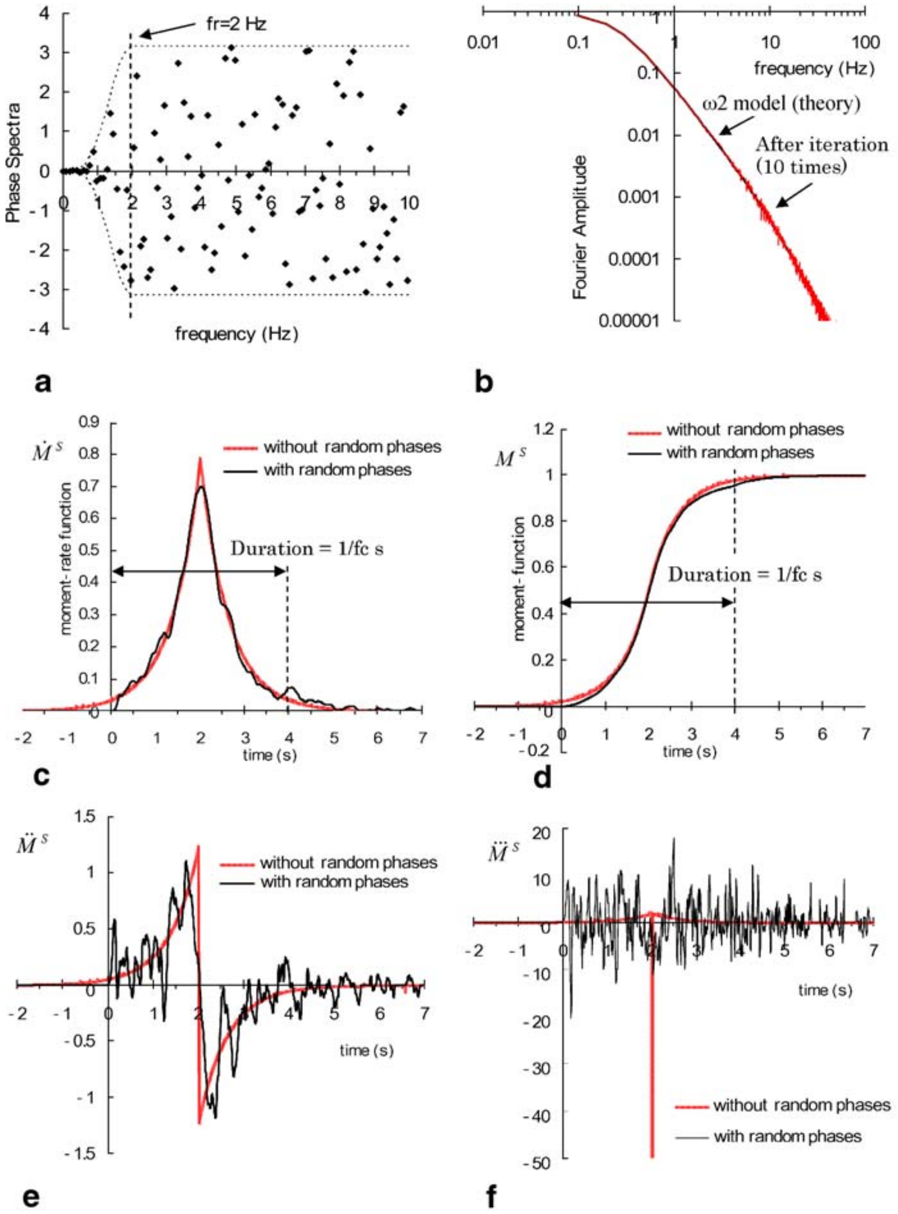

Fig. 3 Moment and moment-rate functions using the broadband stochastic source model (fc=0.25 Hz). **a** Fourier phase spectrum (f_r=2 Hz). **b** Omega-squared Fourier amplitude spectra. **c** Moment-rate function (far-field displacement). **d** Normalized moment function. **e** First derivative of moment-rate function (far-field velocity). **f** Second derivative of moment-rate function (far-field acceleration)

2.3 High-frequency source model for small earthquakes

In this section, we will describe the procedure to introduce the radiation coefficients of P-, SV-, and SH-waves in a layered half-space at high frequencies and to combine these waves with the theoretical radiation pattern of a double couple source at low frequencies. In the case of the far-field in homogeneous media, it is easy to combine the radiation coefficients at high frequencies with the theoretical radiation pattern at low frequencies because the P- and S-waves are expressed independently (e.g., Pitarka et al. 2000).

For the high frequency radiation coefficients, Boore (1983) used the homogenous radiation coefficient of the S-wave (= $\sqrt{2/5}$, Prob. 4.6 in Aki and Richards 1980), by averaging the far-field S-wave over whole focal sphere in a homogenous space. Boore and Boatwright (1984) calculated numerically coefficients of P-, SV-, and SH-waves for various combinations of source and takeoff angles. Recently, Onishi and Horike (2004) derived the analytical radiation coefficients of the P-, SV-, and SH-waves in a homogenous space as follows:

$$\begin{aligned} F_P &= (4/15)^{1/2} \\ F_{\mathrm{SV}} &= \frac{1}{2}\left[\frac{2}{3}\cos^2\lambda\cdot\left\{\frac{2}{5}+\cos^2\delta\right\}\right. \\ &\quad \left.+\frac{1}{3}\sin^2\lambda\cdot\left\{\frac{14}{5}+\sin^2(2\delta)\right\}\right]^{1/2} \\ F_{\mathrm{SH}} &= \frac{1}{2}\left[\frac{2}{3}\cos^2\lambda\cdot\left\{1+\sin^2\delta\right\}\right. \\ &\quad \left.+\frac{1}{3}\sin^2\lambda\cdot\left\{1+\cos^2(2\delta)\right\}\right]^{1/2} \end{aligned} \tag{11}$$

where, δ and λ are the dip and rake angles of a source. F_{P} is the same as Prob. 4.6 in Aki and Richards (1980). It is easily confirmed that the root mean square value of F_{SV} and F_{SH} is equal to the S-wave radiation coefficient ($=\sqrt{2/5}$).

To apply these coefficients to a layered half-space, we need to generate independently the P-, SV-, and SH-waves. We compute them approximately by modifying the representation theorem of Eq. 4. First, we employ the explosive source for generating the P-wave, using the following equation (see Fig. 4a):

$$\dot{U}_k^{\mathrm{S-P}}(X_{\mathrm{O}};\omega) = F_{\mathrm{P}}\cdot\dot{M}^{\mathrm{S}}(\omega)\cdot U_{ik,i}(X_{\mathrm{O}},X_{\mathrm{S}};\omega) \tag{12}$$

Next, we use dip and strike slip sources to generate the SH- and SV-waves, respectively. As shown in Fig. 4b and c, their fault planes are set to be perpendicular to the lines from the source to the observation points. For these cases, the high-frequency waves from the S sources are expressed by the following equations.

$$\dot{U}_k^{\mathrm{S-S}}(X_{\mathrm{O}};\omega) = F_{\mathrm{S}}\cdot\dot{M}^{\mathrm{S}}(\omega)\left(e_i n_j + e_j n_i\right)U_{ik,j}(X_{\mathrm{O}},X_{\mathrm{S}};\omega) \tag{13}$$

where, F_{S} is the radiation coefficient of the SV- and SH-waves in Eq. 11, and the slip vectors (e_i) are those of the dip and strike slip sources shown in the Fig. 4b and c for the SV- and SH-waves, respectively.

It is well know that two horizontal components do not show large differences in amplitudes at high frequencies as compared with those at low frequencies. To make the two horizontal components nearly equal at high frequencies, first, we divide the radial components of the results from the P- and SV-sources equally into the *X*- and *Y*-components by $\sqrt{2}$. Similarly, we divide the transverse components from the SH-source into the two components equally. We generate two sets of the broadband omega-square model with different random phases and use their phases in the two components such that they are independent of each other. Finally, we superpose those high-frequency results with the low frequency results from Eq. 4, by using high-pass and low-pass filters, respectively; we use a trapezoidal filter with tapering amplitudes from one to zero at matching frequencies.

2.4 F-functions and scaling laws of source spectra

It only remains to describe the procedure for selecting the F-function in Eq. 1 to ensure that the scaling law of the source spectra between the small and large

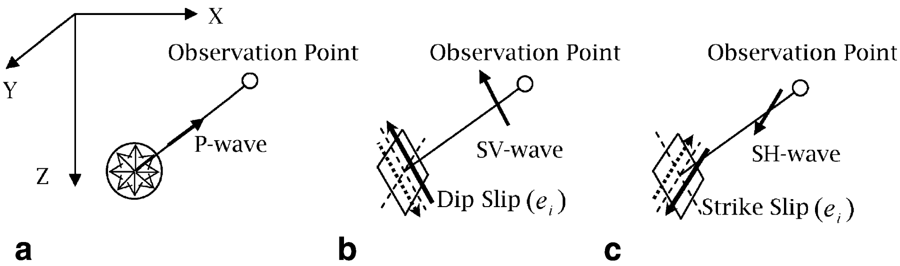

Fig. 4 The explosive, dip, and strike slip sources to generate the high-frequency P-, SV- and SH-waves, respectively. **a** Explosive source. **b** Dip slip source. **c** Strike slip source

earthquakes will be obeyed. Under the assumptions of point sources and the omega-square model with similar values of $f_{\max}$, the scaling law is expressed as follows (e.g., Yokoi and Irikura 1991).

$$\frac{\dot{M}^{\mathrm{L}}(f)}{C\dot{M}^{\mathrm{S}}(f)} \approx \begin{cases} \frac{M_0^{\mathrm{L}}}{CM_0^{\mathrm{S}}} \approx N^3 & (f \to 0) \\ \frac{M_0^{\mathrm{L}}}{CM_0^{\mathrm{S}}} \left(\frac{f_C^{\mathrm{L}}}{f_C^{\mathrm{S}}}\right)^2 = \frac{M_0^{\mathrm{L}}}{CM_0^{\mathrm{S}}} \left(\frac{\Delta\sigma^{\mathrm{L}} M_0^{\mathrm{S}}}{M_0^{\mathrm{L}} \Delta\sigma^{\mathrm{S}}}\right)^{2/3} = \left(\frac{M_0^{\mathrm{S}}}{CM_0^{\mathrm{L}}}\right)^{1/3} \approx N & (f \to \infty) \end{cases} \tag{14}$$

The above scaling law is easily confirmed using Eqs. 2 and 5 for low frequencies and Eqs. 2, 3, 5, and 7 for high frequencies.

We test two types of the F-functions.

$$F(\omega) = 1 + (N-1)\frac{\sin\left(\omega\tau^{\mathrm{L}}/2\beta\right)}{\omega\tau^{\mathrm{L}}/2\beta} \exp\left(\frac{i\omega\tau^{\mathrm{L}}}{2\beta}\right) \tag{15}$$

$$\begin{aligned} F(\omega) &= N \cdot \frac{1 - i\omega\tau^{\mathrm{S}}/\alpha}{1 - i\omega\tau^{\mathrm{L}}/\alpha} \\ &= 1 + (N-1)\frac{1}{1 - i\omega\tau^{\mathrm{L}}/\alpha} \end{aligned} \tag{16}$$

Equation 15 is used in the semi-empirical Green's function method by Irikura (1986), which is the combination of the delta function and the box-car function with a duration of τ^{L}. On the other hand, Eq. 16 is the direct ratio of the slip functions between the small and large earthquakes (Onishi and Horike 2004), in which the exponential function is assumed [$f(t) = \exp(-t/\tau)/\tau$ in the time domain, and $F(\omega) = 1/(1 - i\omega\tau)$ in the frequency domain; Ben-Menahem and Toksoz 1963]. Note that $F \approx N$ for low frequencies ($f \to 0$) and $F \approx 1$ for high frequencies (for $f \to \infty$).

We confirm that Eq. 1, with the use of the two trial F-functions, follows the scaling law of Eq. 14 by using Eqs. 1 and 4.

$$\begin{aligned} \frac{\dot{M}^{\mathrm{L}}(f)}{C\dot{M}^{\mathrm{S}}(f)} &\approx \frac{U_k^{\mathrm{L}}}{CU_k^{\mathrm{S}}} \\ &= \frac{\sum_{\xi=1}^{N}\sum_{\eta=1}^{N} F(\omega) \cdot C_{\xi\eta} \cdot U_{k\xi\eta}^{\mathrm{S}} \cdot \exp\left(i\omega \cdot t_{\xi\eta}\right)}{CU_k^{\mathrm{S}}} \\ &\approx \sum_{\xi=1}^{N}\sum_{\eta=1}^{N} F(\omega) \cdot \exp\left(i\omega \cdot t_{\xi\eta}\right) \end{aligned} \tag{17}$$

where we assume that the focal mechanisms, Green's functions, and the ratios of the stress drops among the small earthquakes are similar. For low frequencies, Eq. 17 is of order N^3 because of the coherent summations of N with respect to ξ (length), η (width), and F (slip $\approx N$). For high frequencies, it becomes of order N because of the random summation of N with respect to ξ and η with $F \approx 1$.

We introduce the free parameters, α and β, in Eqs. 15 and 16 to adjust the durations of the slip functions of the large earthquake. Figure 5a and b shows examples of the Fourier amplitudes of F-functions for the cases of N=10, τ^{L}=1 s, and τ^{L}=10 s. The thin black lines and thick red lines correspond to Eqs. 15 and 16, respectively. All the functions become F=10 (=N) and F=1 at lower and higher frequencies, respectively. Equation 15 shows artificial oscillations due to the presence of the sine function, whereas Eq. 16 shows smooth functions, which indicates that Eq. 16 is more appropriate for practical use. The figures show F-functions for the cases of constant α and β (2β=α=1.0) and the constant $\tau^{\mathrm{L}}/2\beta$ and τ^{L}/α ($\tau^{\mathrm{L}}/2\beta = \tau^{\mathrm{L}}/\alpha = 0.5$). Frequencies between 0.5 and 2 Hz are generally considered to correspond to the boundary between coherent and random phases, and thus, it is probably true that the F-functions reduce their amplitudes from N to 1 within these frequencies. When we use 2β=α=1.0, the F-functions reduce their amplitudes at very low frequencies especially for a large τ^{L} (=10 s, see Fig. 5b).

Figure 6 shows various F-functions of Eq. 16, corresponding to different values of τ^{L}/α. Values from 0.2 to 1.0 of this parameter seem appropriate because they reduce the amplitudes between 0.5 and 2 Hz. Therefore, we recommend the following values for Eqs. 15 and 16.

$$\tau^{\mathrm{L}}/2\beta = \tau^{\mathrm{L}}/\alpha \approx 0.2 - 1.0 \tag{18}$$

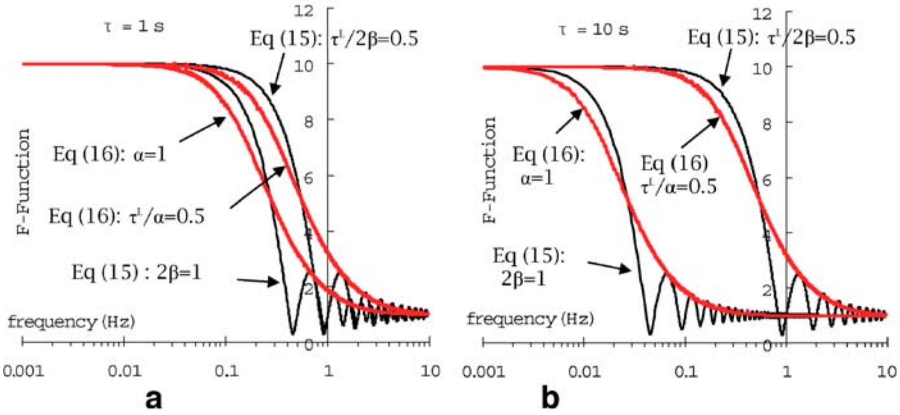

Fig. 5 Examples of F-functions using Eqs. 15 and 16 (N=10). **a** Case for τ^L=1 s. **b** Case for τ^L=10 s

3 Application to strong ground motions of the 1994 Northridge earthquake

3.1 Ground motions of a small earthquake

We apply the proposed method to observed records during the 1994 Northridge earthquake. Before simulating the main motions, we will check ground motions from a small earthquake using various Green's functions. Table 1 shows the material properties for rock (R) and sediment (S) site models (Wald et al. 1996). Table 2 shows the source parameters of a trial small earthquake, and Fig. 7 shows the locations of the source and the three stations, whose epicentral distances are 1, 10, and 100 km along the y-axis. Figure 8 shows the four models whose layered structures correspond to the rock layers of Table 1. Model 1 computes the far-field S-waves at a depth of 4 km under the stations and multiplies the 1-D amplification factor of the S-waves using the overlying three layers. Model 2 computes the P and S-waves in the homogenous full space including the intermediate and near-field terms and multiplies by the 1-D amplification factors of the P- and S-waves for the vertical and horizontal components, respectively. Models 3 and 4 compute the complete waves in the layered half-spaces; Model 3 uses the top four rock layers of Table 1, whereas Model 4 uses all the layers to reproduce the reflection waves from the Conrad and Moho discontinuities.

Figure 9a and b shows the three components of the computed displacements and accelerations, respectively. We use $f_{\max}$=6 Hz and n=1.55 in Eq. 8, the boundary frequency (f_r) between the coherent and random phases is 2 Hz (see Fig. 3a), and the matching frequencies between the theoretical and homogeneous radiation coefficients are 0.5–2.0 Hz. All the waves

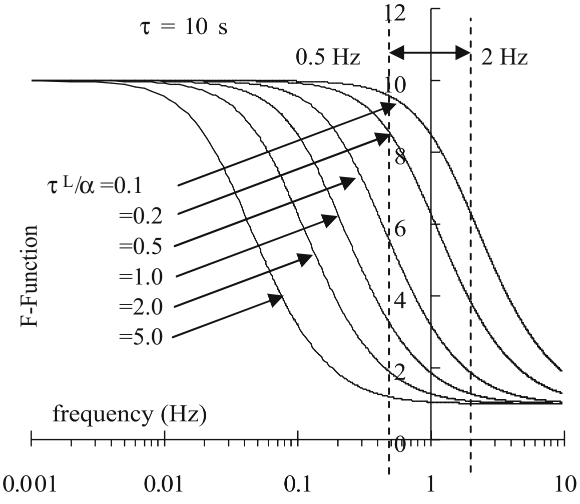

Fig. 6 F-functions using Eq. 16

Table 1 Material properties for the rock and sediment models (Wald et al. 1996)

Layer	Density (kg/m^3)	V_p (m/s)	Q_p	V_s (m/s)	Q_s	Thickness (km)		Depth (km)
						R	S	
1	1,700	800	40	300	20	–	0.1	0.1
2	1,800	1,200	60	500	30	–	0.2	0.3
3	2,100	1,900	100	1,000	50	0.5	0.2	0.5
4	2,400	4,000	200	2,000	100	1.0	1.0	1.5
5	2,700	5,500	400	3,200	200	2.5	2.5	4.0
6	2,800	6,300	400	3,600	200	23.0	23.0	17.0
7	2,900	6,800	600	3,900	300	13.0	13.0	40.0
8	3,300	7,800	600	4,500	300	–	–	

All the Q values are assumed $Q(f) = Q_0 \cdot f^{0.8}$, and $Q(f)>Q_0$, where Q_0 corresponds to Q_P and Q_S in the above table

Table 2 Source parameters of a small earthquake

Depth	Strike	Dip	Rake	$\Delta\sigma$	f_C	M_0	M_W
10 km	122°	40°	100°	100 bar	2 Hz	$6.9\cdot10^{22}$ dyne-cm	4.5

are computed up to 12.5 Hz and high-cut filtered from 10 to 12.5 Hz. Note that the baselines of the waves for Models 1–3 are shifted upward in the figures.

At station 1, which is nearly above the source, the four models show similar results in the horizontal components of motion because the 1-D S-waves are dominant. However, Models 1 and 2 overestimate the horizontal components compared with Models 3 and 4 because they neglect the geometrical attenuations within the upper three layers with the 4-km thickness. In addition, Model 1 shows much smaller amplitudes in the vertical components and smaller horizontal components at lower frequencies (see the EW components of the displacements around 4 s) than those of other models. This is because Model 1 lacks the P-waves and the near-field and intermediate terms of the S-waves. On the other hand, the vertical accelerations of all the models at Station 1 are much smaller than those of the horizontals because the SV and SH sources are dominant in horizontal components than the vertical ones for stations above the source (see Fig. 4b,c). These results appear to contradict those of the empirical relations, in which the vertical accelerations are generally around one half to one third those of the horizontals. Thus, to generate realistic vertical high frequency S-waves at a station above a source, we may need to introduce some modifications in the source models by considering the empirical relations in the future.

As the stations go farther away from the source (Stations 2 and 3), Models 1 and 2 show unrealistic waveforms with much larger amplitudes and shorter durations than those of Models 3 and 4. In particular, they tend to overestimate the vertical components because the SV waves in a simple homogeneous media become dominant in vertical components at a large distance. On the other hand, the results between Models 3 and 4 are almost identical at Stations 1 and 2, whereas Model 4 generates more complicated accelerations at Station 4 than those of Model 3. This is because the reflected waves are generated from the Conrad and Moho discontinuities (e.g., Burger et al. 1987; see accelerations for t>30 s).

3.2 Strong ground motion of the 1994 Northridge earthquake

Finally, we simulate the strong motions during the 1994 Northridge earthquake. Figure 10a shows the locations of the epicenter (the star in the figure), the fault plane, which is dipping toward the southwest, and the observation stations (triangle marks). The white and shaded areas of the figure indicate the rock and sediment areas, respectively, whose structures are shown in Table 1 (Wald et al. 1996). Figure 10b shows the final slip distribution of the strong-motion inversion model by Wald et al. (1996).

We test three models; the first model is identical with the strong-motion inversion model by Wald et al. (1996), where the dislocation time history for each sub-fault is represented by the integral of three isosceles triangles with a duration of 0.6 s and an interval time of 0.4 s. Each triangle is allowed to have different rake angles. We simulate these strong motions up to 1.5 Hz using the layered structures shown in Table 1. The other two models are the same

Fig. 7 Locations of the small earthquake (source point) and the observation stations

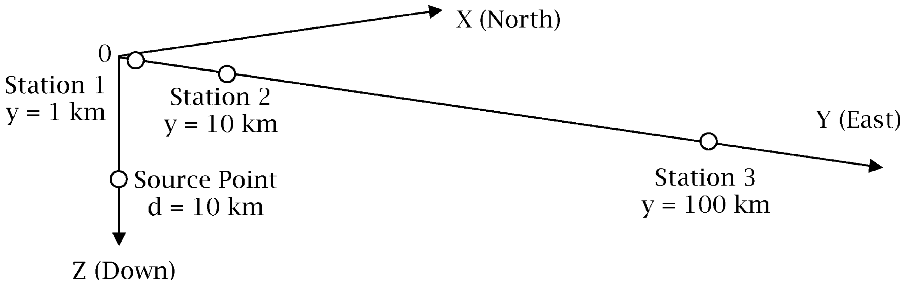

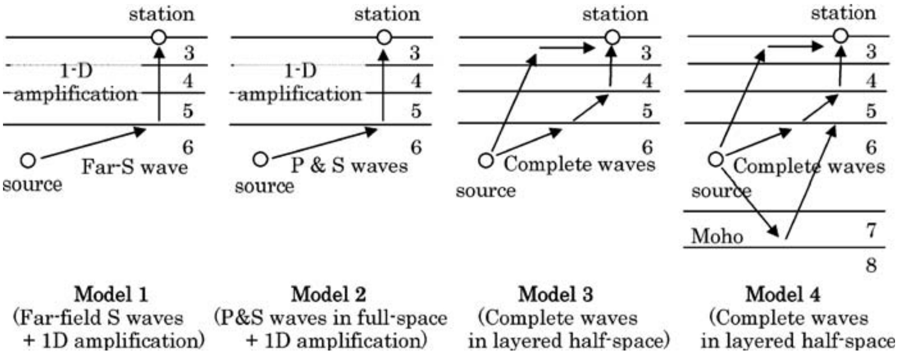

Fig. 8 Four models (the numbers in the layers correspond to those in Table 1). *Model 1* Far-field S waves + 1D amplification). *Model 2* P&S waves in full-space + 1D amplification). *Model 3* Complete waves in layered half-space. Model 4 Complete waves in layered half-space

as Models 2 and 4 in Fig. 8, where we simulate strong motions up to 12.5 Hz and use the high-cut filter from 10 to 12.5 Hz. The followings are the common source parameters in the last two models:

- Scaling parameter: N=14, rupture velocity: V_r=3 km/s
- Ratio of the stress drop between the small and large earthquakes: $C_{\eta\xi} = 1$
- Seismic moments of the small earthquakes in Eq. 6: $M^{\mathrm{S}}_{0\xi\eta} = \mu D^{\mathrm{L}}_{i\xi\eta} LW \big/ N^3$
- Corner frequency of the small earthquake: $f^{\mathrm{S}}_{C\xi\eta}$ in Eq. 7 using $M^{\mathrm{S}}_{0\xi\eta}$
- High-cut filter due to $f_{\max}$: $f_{\max}$=6 Hz, and n=1.55 in Eq. 8
- Boundary frequency between the coherent and random phases: f_r Hz (see Fig. 3a)

Fig. 9 Simulated waves from the small earthquake using the four models of Fig. 8. Note that the baselines of the waves for Models 1–3 are shifted upward. **a** Displacement waves. **b** Acceleration waves

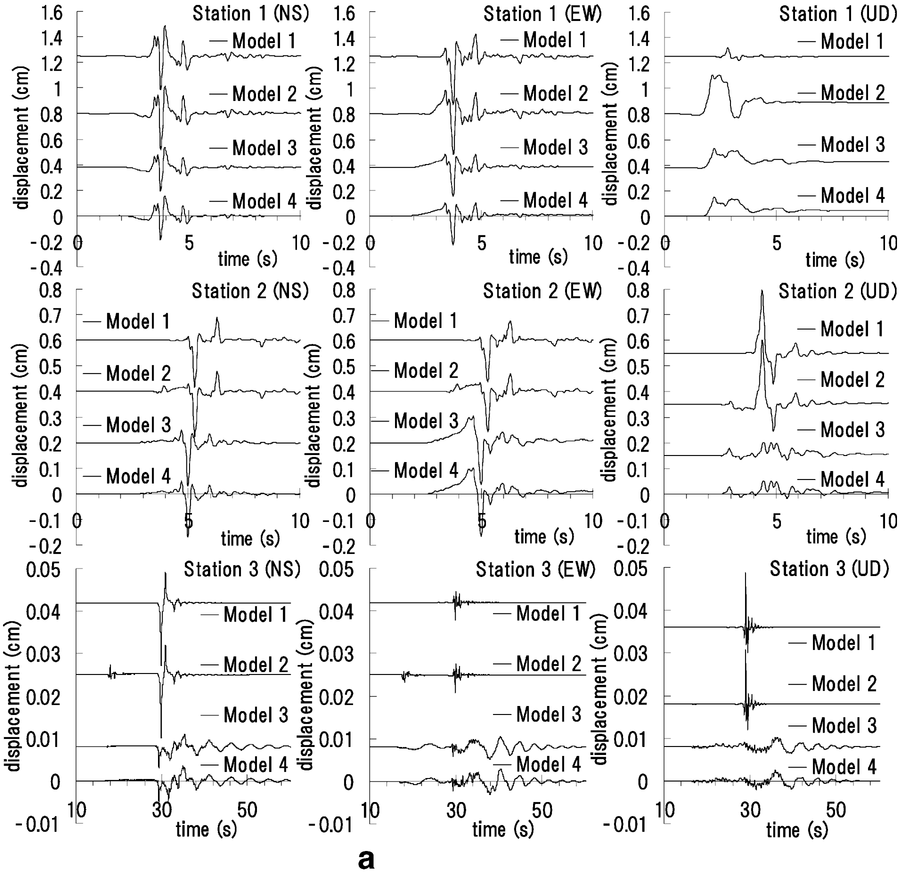

Fig. 9 (continued)

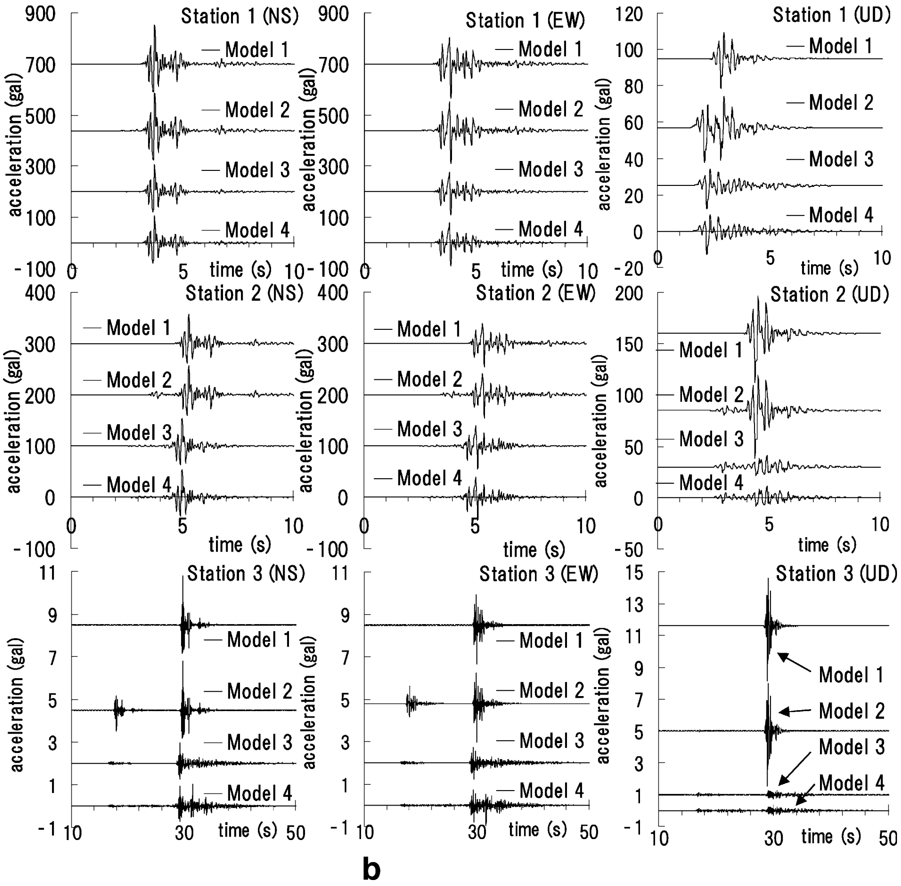

- Matching frequencies from the theoretical to isotropic radiation coefficients: 0.5–2.0 Hz
- F-function and the adjusted rise time: Eq. 16 and $\tau^{\mathrm{L}}/\alpha = 0.5$.

We use the distribution of the final slips and the rake angles of Wald et al. (1996), shown in Fig. 10b. For the stress drop, we use the average values over the fault plane, simply assuming a circular crack model (Eshelby 1957).

$$\Delta\sigma^{\mathrm{L}} = \frac{7\pi^{3/2} M_0^{\mathrm{L}}}{16 S^{3/2}} \tag{19}$$

Fig. 10 1994 Northridge earthquake model and strong motion stations (Wald et al. 1996). **a** Locations of fault, epicenter, and stations. **b** Slip distribution and asperities A1 and A2

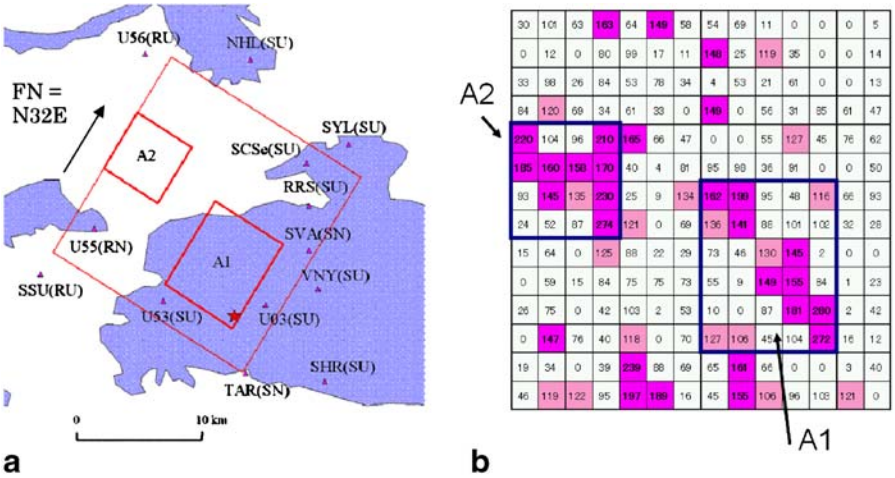

30	101	63	163	64	149	58	54	69	11	0	0	0	5
0	12	0	80	99	17	11	148	25	119	35	0	0	14
33	98	26	84	53	78	34	4	53	21	61	0	0	13
84	120	69	34	61	33	0	149	0	56	31	85	61	47
220	104	96	210	165	66	47	0	0	55	127	45	76	62
185	160	158	170	40	4	81	95	98	36	81	0	0	50
93	145	135	230	25	9	134	162	190	95	48	116	66	93
24	52	87	274	121	0	69	136	141	88	101	102	32	28
15	64	0	125	88	22	29	73	46	130	145	2	0	0
0	59	15	84	75	75	73	55	9	149	155	84	1	23
26	75	0	42	103	2	53	10	0	87	181	280	2	42
0	147	76	40	118	0	70	127	106	45	104	272	16	12
19	34	0	39	239	88	69	65	168	66	0	0	3	40
46	119	122	95	197	189	16	45	155	106	96	103	121	0

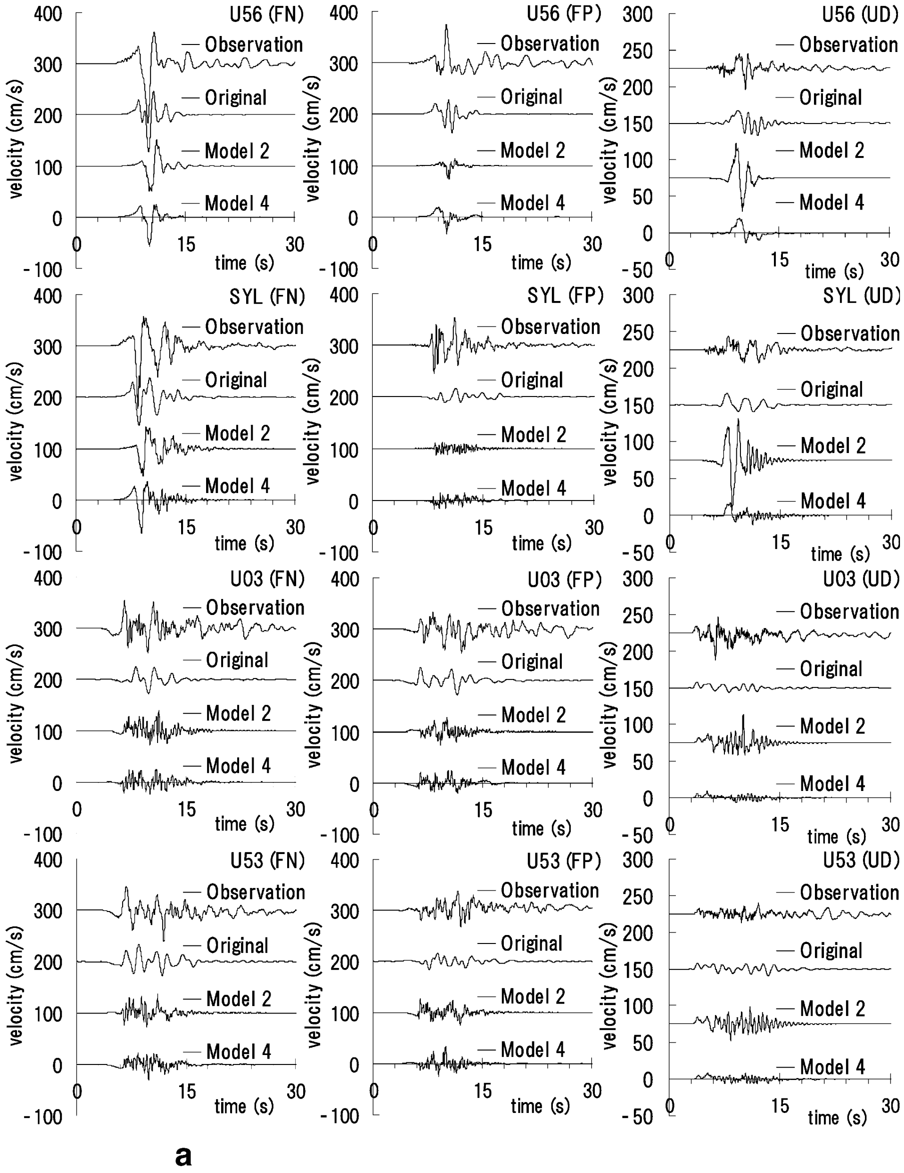

Fig. 11 Observed and simulated waves for the 1994 Northridge earthquake. FN and FP represent the fault normal and parallel components (N32E and N58W), respectively. **a** Observed and simulated velocities at U56, SYL, U03, and U53. **b** Observed and simulated accelerations at U56, SYL, U03, and U53

where, S is the fault area. We obtain $\Delta\sigma$=2.98 MPa (29.8 bar) using $S=L\times W$ m^2 (L=18,000 m, W=24,000 m), and $M_0=1.10\times10^{19}$ N·m.

Due to limited space, we will show results at four stations, U56, SYL, U03, and U53 (see Fig. 10a). Figure 11a and b shows the fault normal (FN, N32E), fault parallel (FP, N58W), and UD components of the velocities and accelerations, respectively, at the four stations. In each case, we plot the observed records (shown as "Observation" in the figures), the simulated results using the original model ("Original"; Wald et al. 1996), and Models 2 and 4 (see Fig. 8). Note that the baselines of the waves for Observation, Original, and Model 2 are shifted upward in the figures.

Because the original model lacks frequencies higher than 1.5 Hz, it reproduces the observed velocities well but not the accelerations. On the other hand, Models 2 and 4 simulate well the horizontal velocities and accelerations of the observations. As for the vertical components, Model 2 generally overestimates the velocities because the SV-waves of Model 2 become dominant in the vertical direction at a certain distance, as seen in Section 3.1 previously.

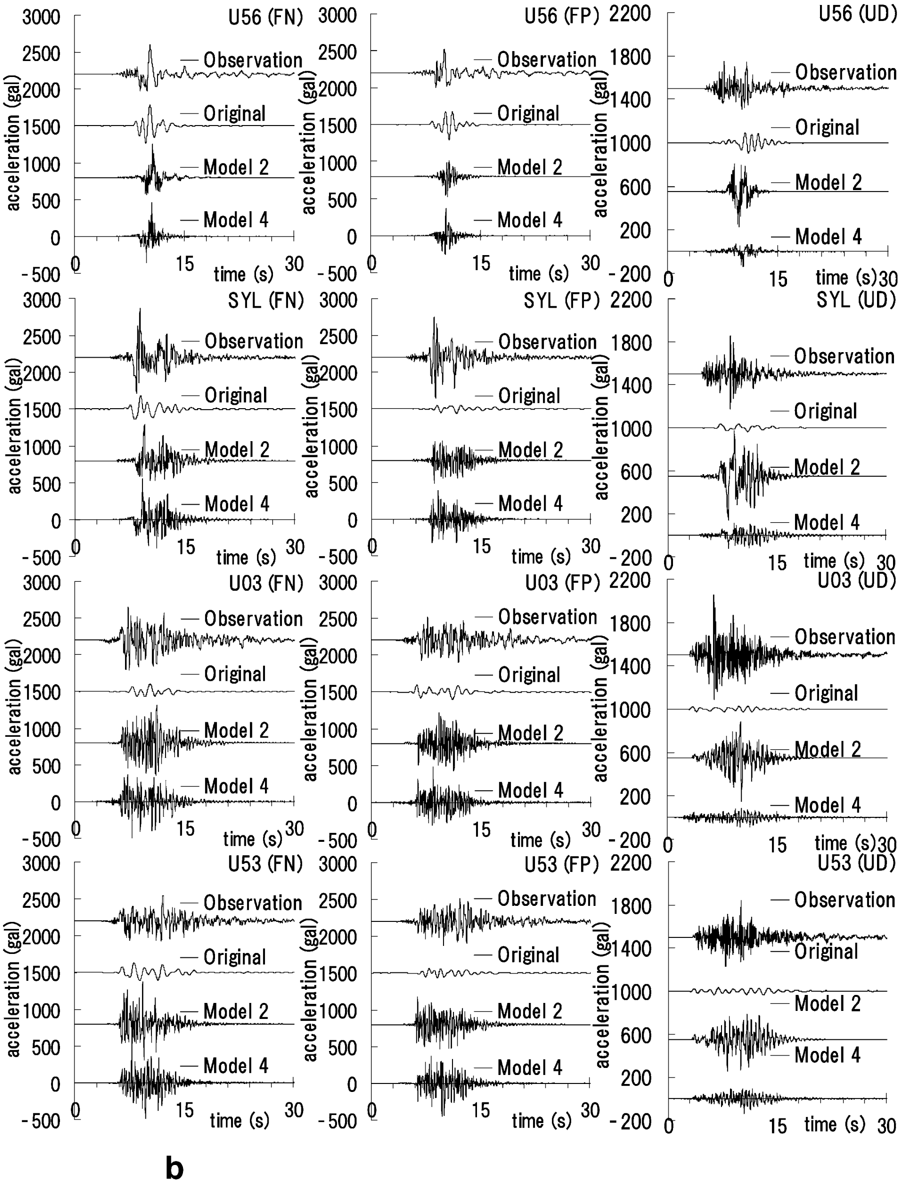

Fig. 11 (continued)

On the contrary, Model 4 tends to underestimate the vertical accelerations because the SV- and SH-waves are dominant on the horizontal components at the stations above sources.

Because U56 and SYL are located at the north of the epicenter, the FN components of their velocities show the forward directivity pulses, namely, large amplitudes and short durations. These coherent waves are successfully reproduced by all the models. On the other hand, the velocity records of U03 and U53 near the epicenter show near random characteristics, namely, smaller amplitudes and longer durations. These waves are also successfully simulated by all the models, although the simulations generally show shorter durations than the observations because they do not include the scattering effects.

Figure 12 shows the Fourier amplitudes of the acceleration records (thick gray lines), the original model (thick black lines), and Models 2 and 4 (thin red and blue lines, respectively). The original model agrees well with the observations at frequencies less than 1 Hz, whereas Models 2 and 4 successfully reproduce the observations at broadband frequencies. In particular, the results of Model 4 are almost

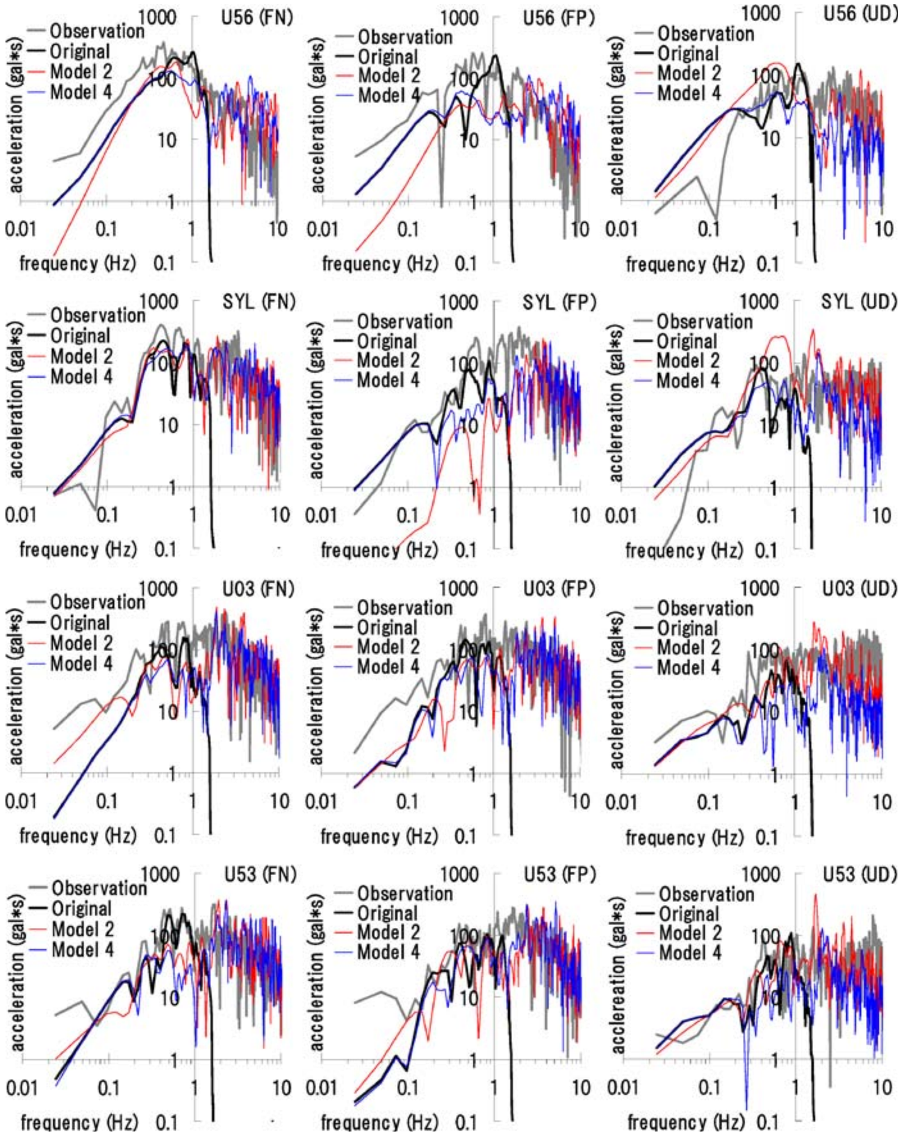

Fig. 12 Observed and simulated Fourier amplitudes of the accelerations at U56, SYL, U03, and U53 for the 1994 Northridge earthquake

identical with those of the original model at frequencies lower than 0.2 Hz, whereas Model 2 is not able to reproduce them (e.g., the FP components at U56 and SYL).

4 Conclusions

We propose a practical method for simulating the three components of broadband P, S, and surface waves in layered half-spaces from an extended fault model, which is an extension of the original stochastic Green's function method (e.g., Kamae et al. 1991). The simulated examples show that the far-field S-waves, which are used in the original method, have imitations not only in the near-field but also in the far-field because they exclude the near and intermediate terms, the surface waves, and the reflected waves from the Moho and Conrad discontinues. We also confirm that the method successfully simulates the observed strong motions of the 1994 Northridge earthquake. On the other hand, we find that the method needs improvements; first, it does not reproduce large amplitudes in vertical high frequency S-waves in the epicentral area because the upward-propagating SV waves are dominant on the horizontal component. The assumption of horizontally flat-layered structures may be an oversimplification in some cases, and we may need to introduce an empirical relation between horizontal and vertical amplitudes. Second, the durations of the simulated waves are generally shorter than those of the observations, although we introduced the complete waves in layered structures. To remedy this problem, we plan to test models in the future that include thin layers to reproduce scattering effects and/or introduce an empirical duration function. Despite these shortcomings, the proposed method will be a more effective tool than the original method for modeling the high frequency contributions in the hybrid methods (e.g., Kamae et al. 1998, Pitarka et al. 2000) because the method reproduces not only stochastic randomness at high frequencies but also deterministic coherencies at low frequencies, using the complete waves in layered half-spaces.

Acknowledgements This research is partly supported by Earthquake and Environmental Research Center (EEC) of Kogakuin University funded by the Frontier Research Promotion Program of the Ministry of Education, Culture, Sports, Science, and Technology of Japan (MEXT) and by the Japan Nuclear Energy Safety Organization (JNES). The manuscript was greatly improved by reviews from Jacobo Bielak, Kim Olsen, and two anonymous reviewers.

References

Aki K, Richards PG (1980) Quantitative seismology. Freeman, New York

Ben-Menahem A, Toksoz MN (1963) Source mechanism from spectrums of long period surface waves. J Geophys Res 68:5207–5222

Boore DM (1983) Stochastic simulation of high-frequency ground motions based on seismological models of the radiated spectra. Bull Seism Soc Am 73:1865–1894

Boore DM, Boatwright J (1984) Average body-wave radiation coefficient. Bull Seism Soc Am 74:1615–1621

Brune JN (1970) Tectonic stress and the spectra of seismic shear waves from earthquake. J Geophys Res 75:4997–5009

Burger RW, Somerville PG et al (1987) The effect of crustal structure on strong ground motion attenuation relations in eastern north America. Bull Seism Soc Am 77:420–439

Eshelby JD (1957) The determination of the elastic field of an ellipsoidal inclusion, and related problems. Proc Roy Soc A241:376–396

Guatteri M, Mai P, Beroza G (2004) A pseudo-dynamic approximation to dynamic rupture models for strong ground motion prediction. Bull Seism Soc Am 94:2051–2063

Hartzell S, Mariagiovanna G et al (2005) Calculation of broadband time histories of ground motion, Part II: kinematic and dynamic modeling using theoretical Green's functions and comparison with the 1994 Northridge earthquake. Bull Seism Soc Am 95:614–645

Herrero A, Bernard P (1994) A kinematic self-similar rupture process for earthquake. Bull Seism Soc Am 84:1216–1228

Hisada Y (1995) An efficient method for computing Green's functions for a layered half-space with sources and receivers at close repths (Part 2). Bull Seism Soc Am 85:1080–1093

Hisada Y (2000) A theoretical omega-squared model considering the spatial variation in slip and rupture velocity. Bull Seism Soc Am 90:387–400

Hisada Y (2001) A theoretical omega-squared model considering the spatial variation in slip and rupture velocity. Part 2: case for two-dimensional source model. Bull Seism Soc Am 91:651–666

Irikura K (1983) Semi-empirical estimation of strong ground motions during large earthquakes. Bull Disas Prev Res Inst 33:63–104

Irikura K (1986) Prediction of strong ground acceleration motions using empirical Green's function. Proc 7th Japan Earthq Eng Symp, pp 151–156

Kagawa T (2004) Developing a stochastic Green's function method having more accuracy in long period range to be used in the hybrid method. J Jpn Assoc Earthqu Eng 4: 21–32 (in Japanese)

Kamae K, Irikura K, Fukuchi Y (1991) Prediction of strong ground motion based on scaling law of earthquake by stochastic synthesis method. J Struct Constr Eng Trans AIJ No430:1–9 (in Japanese)

Kamae K, Irikura K, Pitarka A (1998) A technique for simulating strong ground motion using hybrid Green's function. Bull Seism Soc Am 88:357–367

Onishi Y, Horike M (2004) The extended stochastic simulation method for close-fault earthquake motion prediction and comments for its application to the hybrid method. J Struct Constr Eng Trans AIJ 586:37–44

Pitarka A, Somerville P et al (2000) Simulation of near-fault ground-motion using hybrid Green's functions. Bull Seism Soc Am 90:566–586

Tsuruki M, Kagawa T et al (2006) Study on a high-cut filter for strong ground motion prediction – based on the observed records during the 1995 Hyogo-ken Nambu Earthquake. J Jpn Assoc Earthqu Eng 6:94–112 (in Japanese)

Wald DJ, Heaton TH, Hudnut KW (1996) The slip history of the 1994 Northridge, California, earthquake determined from strong motion, teleseismic, GPS, and leveling data. Bull Seism Soc Am 86:49–70

Yokoi T, Irikura K (1991) Empirical green's function technique based on the scaling law of source spectra. J Seism Soc of Japan Second Series, 44:109–122 (in Japanese)